Contents lists available at ScienceDirect

Applied Catalysis B: Environmental

Fe$_x$Co$_{3-x}$O$_4$ nanocages derived from nanoscale metal–organic frameworks for removal of bisphenol A by activation of peroxymonosulfate

Xuning Li [a,b], Zhaohui Wang [c,d], Bo Zhang [a], Alexandre I. Rykov [a], Mamdouh A. Ahmed [e], Junhu Wang [a,*]

[a] Mössbauer Effect Data Center & Laboratory of Catalysts and New Materials for Aerospace, Dalian Institute of Chemical Physics, Chinese Academy Sciences, Dalian 116023, China
[b] University of Chinese Academy of Sciences, Beijing 100049, China
[c] State Environmental Protection Engineering Center for Pollution Treatment and Control in Textile Industry, College of Environmental Science and Engineering, Donghua University, Shanghai 201620, China
[d] Southern Cross GeoScience, Southern Cross University, Lismore, NSW 2480, Australia
[e] Physics Department, Faculty of Science, Al Azhar University, Nasr City, Cairo, Egypt

ARTICLE INFO

ABSTRACT

Here we report a facile strategy to synthesize porous Fe$_x$Co$_{3-x}$O$_4$ nanocages by heating Prussian blue analogues Fe$_y$Co$_{1-y}$[Co(CN)$_6$]$_{0.67}$·nH$_2$O nanospheres with tunable size and morphology. The iron doping amount had significant influence on the final morphology and the most uniform nanocages were obtained from $x = 0.8$. The catalytic performance of the nanocages was thoroughly evaluated by activation of peroxymonosulfate (PMS) for removal of bisphenol A (BPA) in water. The influence of different process parameter on the BPA degradation efficiency was examined and the catalytic stability was tested. The BPA degradation pathway was proposed based on GC–MS and LC–MS results. The involved radicals were identified through radical scavenging experiments and electron paramagnetic resonance spectroscopy. Mössbauer and XPS techniques were applied to illustrate the catalytic mechanism and B-site Co^{II} on the surface of Fe$_x$Co$_{3-x}$O$_4$ nanocages was determined as the main factor for PMS activation. Results indicate that porous Fe$_x$Co$_{3-x}$O$_4$ nanocages are available to serve as alternative environmentally friendly catalysts for pollutants removal by activation of PMS.

© 2015 Elsevier B.V. All rights reserved.

1. Introduction

As one of the most common organic pollutants in wastewater, bisphenol A (BPA) is an extensively used chemical in bottles, packaging, plastics, paper and epoxy resins [1]. Considered as an endocrine-disrupting compound (EDC), BPA is detrimental to the development of the reproductive organs when accumulated in the human body [2]. Traditional treatments such as biological treatment [3], adsorption [4], and photocatalytic treatment [5] are usually constrained by at least one of the disadvantages such as slow process, secondary waste and high cost, etc. Therefore, it is urgent to develop effective methods to remove BPA from the contaminated environment.

Hydroxyl radical (HO•), generated from the Fenton or Fenton-like process, is highly efficient to degrade nearly all organic compounds [6,7]. However, the Fenton process requires an acidic pH condition and also leads to massive sludge production, remarkably limiting their practical applications. Although heterogeneous Fenton process could overcome these drawbacks, it still has relatively low efficiency in terms of both long reaction time and low utilization rate of H$_2$O$_2$ [8–10]. Compared to HO• with standard reduction potential of 1.8–2.7 V, sulfate radicals (SO$_4$•$^-$) are more active for oxidation with higher reduction potential of 2.5–3.1 V [11]. Cobalt was found to be very active to produce SO$_4$•$^-$ by activating peroxymonosulfate (PMS) for pollutants degradation [12]. To date, various cobalt containing catalysts have been developed to activate PMS [13–24]. For instance, Yang et al. reported the critical roles of iron in catalytic activity and separation of CoFe$_2$O$_4$ [13]. Su et al. found that the higher cobalt content in the catalyst was benefit for the removal of Rhodamine B by activation of PMS [18]. It was also found that the CoFe$_2$O$_4$ had the highest catalytic activ-

ity on di-n-butyl phthalate degradation among MFe_2O_4 (M = Co, Cu, Mn, and Zn) [19]. However, all these reported catalysts contain less cobalt when compared to the amount of iron. Fabricating $Fe_xCo_{3-x}O_4$ ($0 < x < 1.0$) catalysts with high Co content is therefore very critical for efficient activation of PMS.

At present, numbers of approaches have been employed to synthesize mixed transition-metal oxides (MTMOs), including sol–gel [25], co-precipitation [26], thermal decomposition [27], and so on. In general, a high surface area usually results in high activity for the surface catalytic reaction. However, despite continuous efforts, the facile strategy to fabricate porous MTMOs nanoparticles with relative high surface area still remains challenging. In our previous work, we have developed $Fe_3[Co(CN)_6]_2 \cdot 12H_2O$ and $Fe[Co(CN)_6] \cdot 2H_2O$ Prussian blue analogues (Fe–Co PBAs) as excellent photo-Fenton catalysts [28]. Although CN^- is closely associated with stable $[Co(CN)_6]^{3-}$ complex, one may prefer to use oxide in place of cyanide catalysts. In this case, it is desirable to remove CN^- from Fe–Co PBAs while retaining their excellent catalytic activity. Recently, porous nanostructured oxides derived from nanoscale metal–organic frameworks (MOFs) were widely investigated [29–32], which showed that the original morphology of MOFs could be almost retained even after a thermal treatment. As the MTMOs have recently attracted increasing research interest worldwide [33], and the addition of cationic impurities could realize morphology control, we consider the cation doped PBAs with controllable morphology as the novel potential precursors for porous MTMOs. Moreover, the porous MTMOs may have great potential to serve as highly efficient heterogeneous catalysts for pollutants removal by activation of PMS.

In the present work, a facile strategy was developed to synthesize porous $Fe_xCo_{3-x}O_4$ ($0 < x < 1.0$) nanocages by heating the designed precursors of $Fe_yCo_{1-y}[Co(CN)_6]_{0.67} \cdot nH_2O$ (Fe_yCo_{1-y}-Co PBAs) nanospheres. The crystalline structure, morphology and textural property of the prepared $Fe_xCo_{3-x}O_4$ nanocages were thoroughly characterized by various techniques. The catalytic performance of the nanocages was evaluated by activation of PMS for removal of BPA. The influence of different process parameter on the BPA degradation efficiency was examined and the catalytic stability was tested. The BPA degradation pathway was studied and the involved radical intermediates ($SO_4^{\bullet-}$, $HO^{\bullet}$) were identified. The mechanism of PMS activated by the catalysts was explored by X- ray photoelectron spectroscopy (XPS) and ^{57}Fe Mössbauer spectroscopy.

2. Experimental

2.1. Chemicals

Potassium hexacyanocobaltate(III) (98%) and cobaltosic oxide (98.5%) were purchased from Beijing J&K Co., Ltd, China. PMS ($KHSO_5 \cdot 0.5KHSO_4 \cdot 0.5K_2SO_4$) was purchased from Alfa Aesar. BPA, 5,5-dimethyl-1-pyrroline-N-oxide (DMPO) and iron oxide (II,III) (99.5%, ~20 nm) were purchased from Aladdin Co., China. Sodium sulfite, ferrous chloride, cobaltous chloride, poly(vinylpyrrolidone) (PVP), t-butanol (TBA) and methyl alcohol were purchased from Tianjin Kermel Chemical Reagent Co., Ltd, China. All chemical reagents were used without further purification.

2.2. Sample preparation

Fe_yCo_{1-y}-Co PBAs nanospheres were prepared by the reaction of $FeCl_2 \cdot 4H_2O$ and $CoCl_2 \cdot 6H_2O$ mixture with $K_3[Co(CN)_6]$ in PVP aqueous solution. Typically, desired amounts of $FeCl_2 \cdot 4H_2O$ and $CoCl_2 \cdot 6H_2O$ (totally 9 mM) were dissolved in 40 mL deionized water with PVP (1.2 g) under vigorous stirring. Then 40 mL $K_3[Co(CN)_6]$

aqueous solution (5 mM) was slowly added into the premixed solution. The obtained colloid solution was further stirred for another 30 min and aged for 20 h. The resulting precipitates were centrifuged and washed for at least three times with the mixture of ethanol and deionized water, followed by drying in an oven at 333 K for 20 h. To obtain the $Fe_xCo_{3-x}O_4$ ($0 < x < 1.0$) nanocages, Fe_yCo_{1-y}-Co PBAs nanospheres were heated at 773 K and kept for 1 h in air (Scheme 1).

2.3. Characterization

The X-ray diffraction (XRD) patterns were collected on a PANalytical X'Pert-Pro X-ray diffractometer equipped with Cu Kα ($\lambda = 0.15406$ nm) radiation source in a 2θ range from $10°$ to $80°$. The morphologies and structures of the samples were characterized by field-emission scanning electron microscopy (FESEM, JSM 7800F) and high-resolution transmission electron microscopy (HR-TEM, JEM-2100F). The $Fe_xCo_{3-x}O_4$ nanocages were dissolved in aqua regia to analyze the sample compositions, using Thermo IRIS Interepid II inductively coupled with plasma-optical emission spectroscopy (ICP-OES). The specific surface areas were analyzed on a Micromeritics ASAP 2010 instrument with the Brunauer–Emmett–Teller (BET) N_2 adsorption–desorption method at 77 K, and the pore size distributions were analyzed by the Barrett–Joyner–Halenda (BJH) method. The thermo-gravimetric and differential scanning calorimetry (TG-DSC) analyses were collected on a Setaram Setsys 16/18 thermo-analyzer at a heating rate of 10 K min^{-1} in air flow. The X-ray photoelectron spectra (XPS) were recorded on the ESCALAB 250 X-ray photoelectron spectroscope equipped with monochromated Al Kα source. The spectra were fitted by XPSPEAK41 software using Shirley-type background. The room temperature ^{57}Fe Mössbauer spectra were collected using a Topologic 500 A spectrometer and a proportional counter with ^{57}Co (Rh) as a γ-ray radioactive source. The EPR spectra obtained by a Brucker EPR I200 spectrometer with a center field at 3320 G and a sweep width of 100 G at room temperature. The detailed procedures of Mössbauer and EPR measurements can be found in our previous work [34].

2.4. Catalytic activity measurements

The catalytic performance of the nanocages was evaluated by activation of PMS (0.2 g L^{-1}) for removal of BPA in water (20 mg L^{-1}) at pH 6.0 in a dark box. The reaction temperature was kept at 298 K. If necessary, the pH value was adjusted by either 0.1 M NaOH or HNO_3 aqueous solution and recorded by an Orion pH meter (model PHSJ-3F). The concentrations of leached iron and cobalt were measured by ICP-OES.

In all experiments, 5 mg catalyst was added into a 50 mL BPA solution (20 mg L^{-1}) and stirred for 30 min to establish the adsorption–desorption equilibrium. The reaction was initiated by adding certain amounts of PMS aqueous solution. At given reaction time intervals, samples (1 mL) were withdrawn, immediately quenched with 0.5 mL methanol and then centrifuged. In each recyclability test, the catalyst was collected using a magnet and washed thoroughly with deionized water.

The concentration of BPA was analyzed by a high performance liquid chromatography (HPLC, Agilent, 1260-Infinity) with a C18 column. The mobile phase was methanol/water mixture (70:30, v/v) with a flow rate at 0.6 mL min^{-1}. The detection wavelength was set at 230 nm. The total organic carbon (TOC) values were determined by a total organic carbon analyzer (TOC-VCPH/CPN, Shimadzu, Japan). The BPA degradation intermediates were identified by GC–MS (Varian 450GC-320 MS) and LC–MS. GC–MS was performed with a FID detector and HP-5 capillary column. Prior to the analysis, 50 mL reaction mixture was centrifuged and extracted
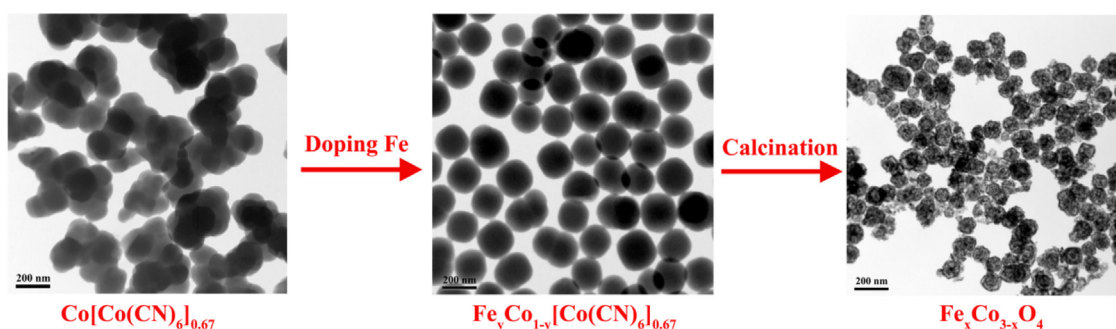
Scheme 1. Preparation procedure of $Fe_xCo_{3-x}O_4$ nanocages.

with dichloromethane three times. The extracted solution was then concentrated to about 1 mL before analysis. LC–MS was performed on an Agilent 6540 quadrupole time-of-flight mass spectrometer in combination with an Agilent 1290 Infinity ultrahigh-performance liquid chromatography system with Agilent ZORBAX Eclipse Plus C18 column.

The reaction rate was evaluated by a first order kinetics model as the following equation:

$$\ln \left(\frac{C_0}{C_t} \right) = kt$$

where C_0 is the initial pollutant concentration, C_t is the concentration at a certain time t during the degradation process, and k is the reaction rate constant.

3. Results and discussion

3.1. Characterization of Fe_yCo_{1-y}-Co PBAs nanospheres and $Fe_xCo_{3-x}O_4$ nanocages

Fig. 1 shows representative TEM images of Fe_yCo_{1-y}-Co PBAs. There was no uniform morphology for Co–Co PBA (Fig. 1a), however, the morphology became more and more uniform with tunable sizes (100–200 nm) when increasing iron doping amount (Fig. 1b–f). As is known, the cationic doping could induce the change in the crystal structure and is useful for controlling the solution growth of the nanoparticles [35], which is most probably the reason for such a significant influence on the final morphology through iron doping. Fig. 2 shows XRD patterns of Fe_yCo_{1-y}–Co PBAs. All the characteristic diffraction peaks could be assigned to $Co_3[Co(CN)_6]_2 \cdot nH_2O$ (JCPDS No. 22-0215). No other impurity diffraction peaks were detected, indicating the high purity of the products.

The as-prepared Fe_yCo_{1-y}-Co PBAs nanospheres could be transformed into $Fe_xCo_{3-x}O_4$ nanocages after heating in air at 773 K. As indicated in TG analysis (Fig. S1), the decomposition process of Co–Co or Fe–Co PBA was divided into two stages, and the total weight loss rate was ca. 47.2% or 44.9%, respectively. The weight loss in the first stage (below 553 K) was due to the removal of the crystalline and coordinated water. The following weight loss (over 553 K) was due to the decomposition of the organic ligands (C—N). In this process, the Fe_yCo_{1-y}-Co PBAs were decomposed into $Fe_xCo_{3-x}O_4$ and the organic ligands were oxidized into gases (CO_2, NO_x, etc.).

The crystallographic structure and phase purity of the hollow porous $Fe_xCo_{3-x}O_4$ nanocages were characterized by XRD (Fig. 3). All the characteristic diffraction peaks were identical to those of spinel Co_3O_4 (JCPDS No. 42-1467). The slight shift of the peak positions towards smaller angles indicates the presence of Fe doping in as-prepared materials.

Table 1
The composition and average crystallite size of $Fe_xCo_{3-x}O_4$ nanocages.

Nanocages	Metal content (mol% × 3)		Average crystallite size
	Fe	Co	(nm)
$Fe_{0.2}Co_{2.8}O_4$	0.21	2.79	20.4
$Fe_{0.3}Co_{2.7}O_4$	0.34	2.66	16.1
$Fe_{0.5}Co_{2.5}O_4$	0.51	2.49	15.2
$Fe_{0.7}Co_{2.3}O_4$	0.68	2.32	13.9
$Fe_{0.8}Co_{2.2}O_4$	0.78	2.22	13.3

The average crystallite size of $Fe_xCo_{3-x}O_4$ was calculated using the Debye–Scherrer equation and the composition was analyzed by ICP (Table 1). Fig. 4a–e shows the SEM images of $Fe_xCo_{3-x}O_4$ with different Fe doping amount. It is interesting to note that the morphology of $Fe_xCo_{3-x}O_4$ almost retained even after the thermal treatment of Fe_yCo_{1-y}-Co PBAs. With the increase of Fe doping amount, the particle size increased from about 80 to 160 nm and the morphology became more and more uniform. The TEM image of $Fe_{0.8}Co_{2.2}O_4$, which appeared to be the most uniform, is shown in Fig. 4f. In particular, a typical structure with thin shell and well-defined interior like nanocages could be detected. The porous structure was caused by the rapid mass-transport across the shells during heating. Furthermore, the surface of the synthesized $Fe_xCo_{3-x}O_4$ was assembled from nanosized particles, which was in good accordance with the XRD results. Fig. 5a–b shows the HR-TEM images of $Fe_{0.8}Co_{2.2}O_4$, the lattice spacings of 0.25 nm and 0.21 nm were correspond well to the spinel-type Co_3O_4 (3 1 1) and (4 0 0) planes, respectively [36]. In addition, the element mapping clearly illustrates the homogeneous distribution of Fe, Co and O species in the porous $Fe_xCo_{3-x}O_4$ nanocages (Fig. 5c–f).

Previously, Hu et al. fabricated $Fe_xCo_{3-x}O_4$ porous nanostructure which involved a morphology conserved from $Fe_3[Co(CN)_6]_2 \cdot nH_2O$ PBA [37]. However, limited to the Fe/Co ratio in PBA, only $Fe_{1.8}Co_{1.2}O_4$ spinel (about 1 μm) could be obtained from such strategy. The constant ratio of transition metals in PBAs largely limited the application of this method [38,39]. Therefore, in our novel method, using cationic doped PBAs with controllable morphology as precursors may have great potential for the porous MTMOs preparation. The porosity of the $Fe_xCo_{3-x}O_4$ nanocages was determined by N_2 adsorption–desorption measurement (Fig. S2). The type IV isotherm with H3-shaped hysteresis loops indicating the presence of mesopores (around 5 nm), which was consistent with the SEM and TEM results. The BET surface area of the $Fe_{0.8}Co_{2.2}O_4$ nanocages (62 $m^2 g^{-1}$) is higher than those of the reported spinel-type catalysts [40,41]. In addition, combine with the magnetic behavior of $Fe_{0.8}Co_{2.2}O_4$ (Fig. S3), $Fe_xCo_{3-x}O_4$ nanocages may have great potential applications for pollutants degradation by activation of PMS.
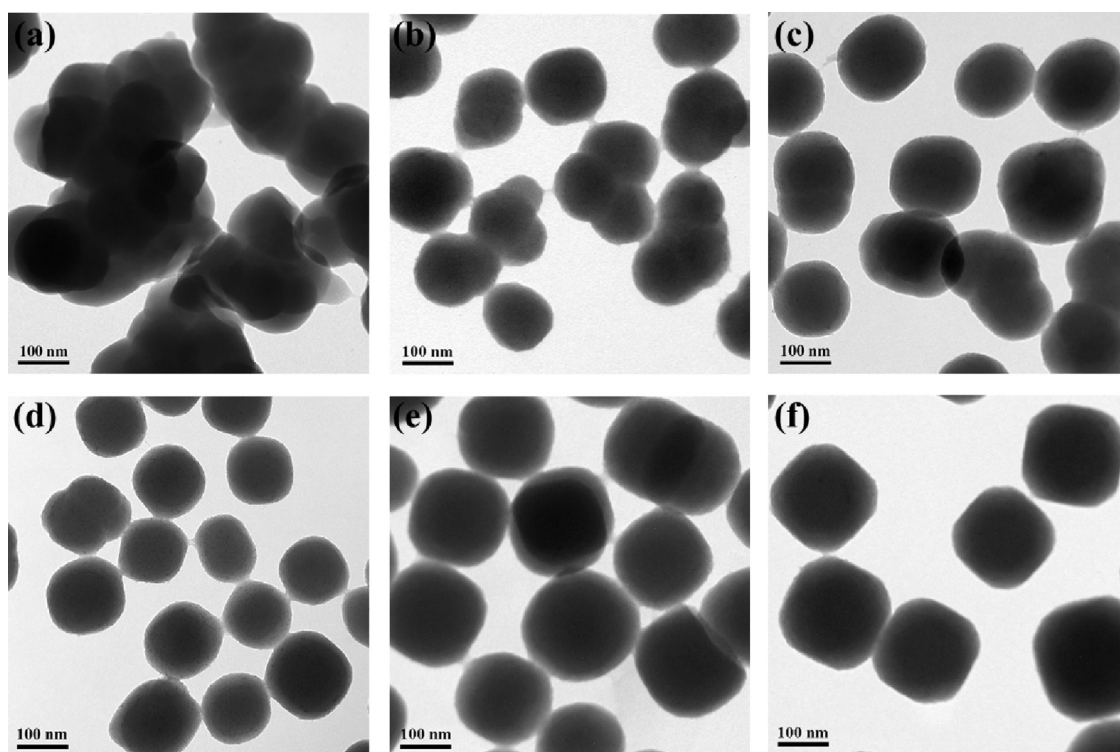
Fig. 1. TEM images of Fe_yCo_{1-y}-Co PBAs: (a) Co–Co PBA, (b) $Fe_{0.1}Co_{0.9}$−Co PBA, (c) $Fe_{0.2}Co_{0.8}$−Co PBA, (d) $Fe_{0.3}Co_{0.7}$-Co PBA, (e) $Fe_{0.4}Co_{0.6}$-Co PBA, (f) $Fe_{0.5}Co_{0.5}$−Co PBA.
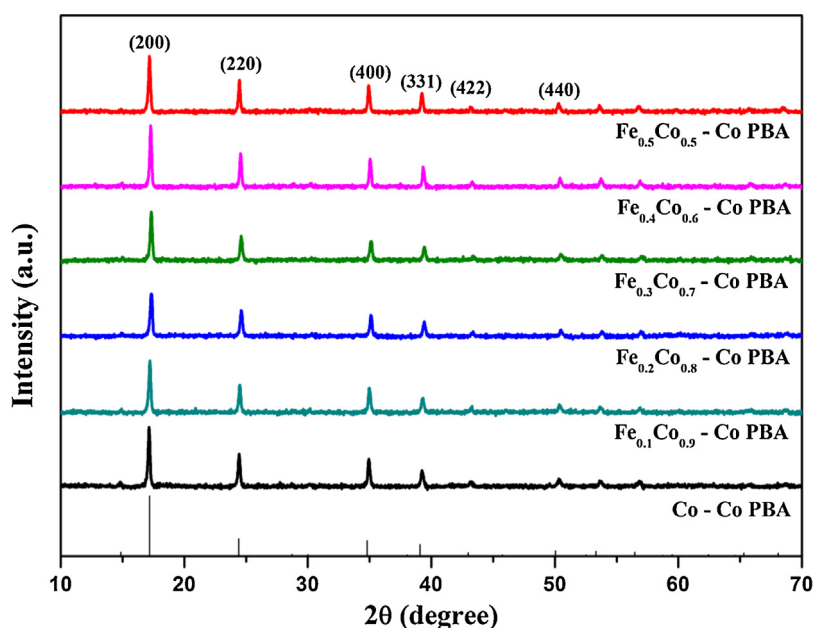
Fig. 2. XRD patterns of Fe_yCo_{1-y}-Co PBAs.

3.2. Catalytic performance and stability of $Fe_xCo_{3-x}O_4$ nanocages

The catalytic performance of the nanocages was studied by activation of PMS for removal of BPA using $Fe_{0.8}Co_{2.2}O_4$ as a model. Fig. 6 presents the removal profiles of BPA under various reaction systems. A control test using only $Fe_{0.8}Co_{2.2}O_4$ nanocages shows that less than 3% of BPA was adsorbed in 60 min, revealing its negligible adsorption capacity. In addition, only PMS also could not induce significant BPA degradation. Less than 10% of BPA was degraded, indicating that thermal activation of PMS for

production of reactive radicals was negligible at current reaction conditions. The simultaneous presence of $Fe_{0.8}Co_{2.2}O_4$ nanocages and PMS led to a significant enhancement of the BPA removal efficiency as compared to the adsorption and oxidation with PMS alone. As high as 95% BPA removal efficiency could be achieved within 60 min, despite using low catalysts concentration ($0.1\,g\,L^{-1}$). In addition, the leaching solution only resulted in a removal of 13% of BPA (Fig. S4), indicating that the BPA degradation is mainly induced by heterogeneous catalytic reaction over $Fe_{0.8}Co_{2.2}O_4$ surface. The catalytic activity of $Fe_{0.8}Co_{2.2}O_4$ was comparable to those
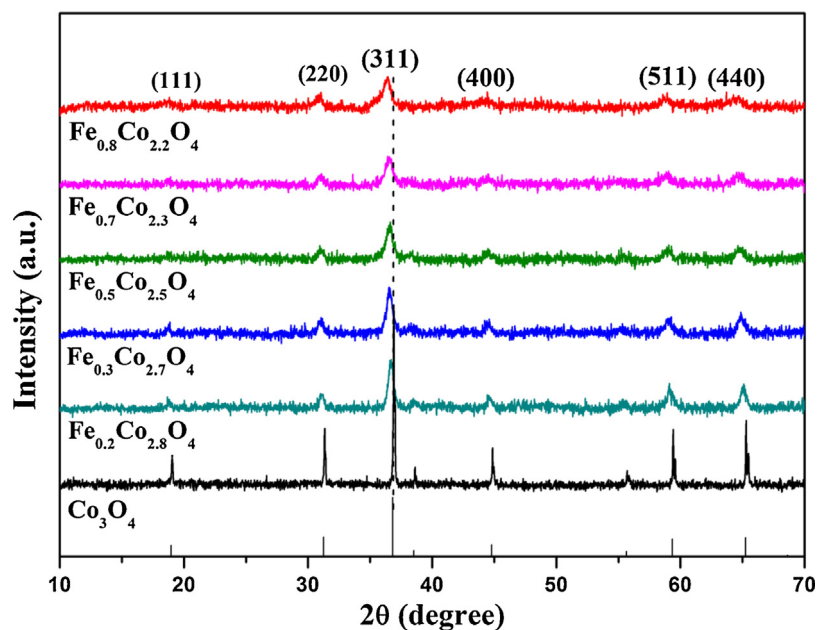
Fig. 3. XRD patterns of $Fe_xCo_{3-x}O_4$ nanocages.
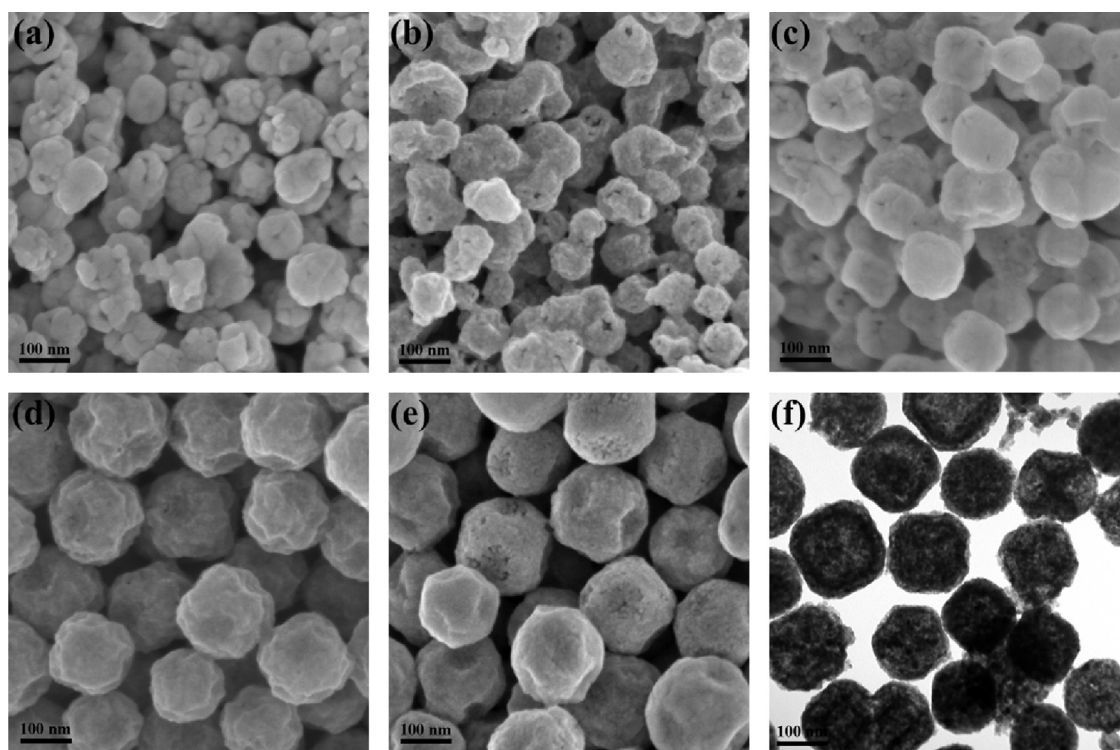
Fig. 4. SEM images of $Fe_xCo_{3-x}O_4$ nanocages (a) $Fe_{0.2}Co_{2.8}O_4$, (b) $Fe_{0.3}Co_{2.7}O_4$, (c) $Fe_{0.5}Co_{2.5}O_4$, (d) $Fe_{0.7}Co_{2.3}O_4$, (e) $Fe_{0.8}Co_{2.2}O_4$; (f) TEM image of $Fe_{0.8}Co_{2.2}O_4$.

Fe-/Co-based catalysts recently reported in the literatures (Table S1) [13,21,22,42–44], and much higher compared to the commercial Fe_3O_4 and Co_3O_4, which provided 7% and 24% BPA removal efficiency, respectively.

Previous researches have reported that the removal of BPA by activation of PMS followed a first-order kinetic model. In this study, the BPA removal kinetics could be fitted well by the first-order kinetics as shown in Fig. S5. The apparent rate constant (k) was $0.049\,min^{-1}$ under the present conditions ($R^2 = 0.998$), which is much higher than those of the reported catalysts for the BPA

removal by activation of PMS [42]. In addition, temperature dependence of BPA degradation efficiency indicates the endothermic nature of PMS activation process (Fig. S6). As shown in Fig. 7a, about 39% of BPA was mineralized in 60 min, suggesting that BPA was not only degraded to small organic compounds, but even mineralized to inorganic carbon forms.

The influence of initial pH on BPA removal efficiency was studied in the process of PMS oxidation (Fig. 7b). It was obvious that the values of k increased from $0.035\,min^{-1}$ to $0.051\,min^{-1}$ when the solution pH increased from 4.0 to 8.0. However, further increase

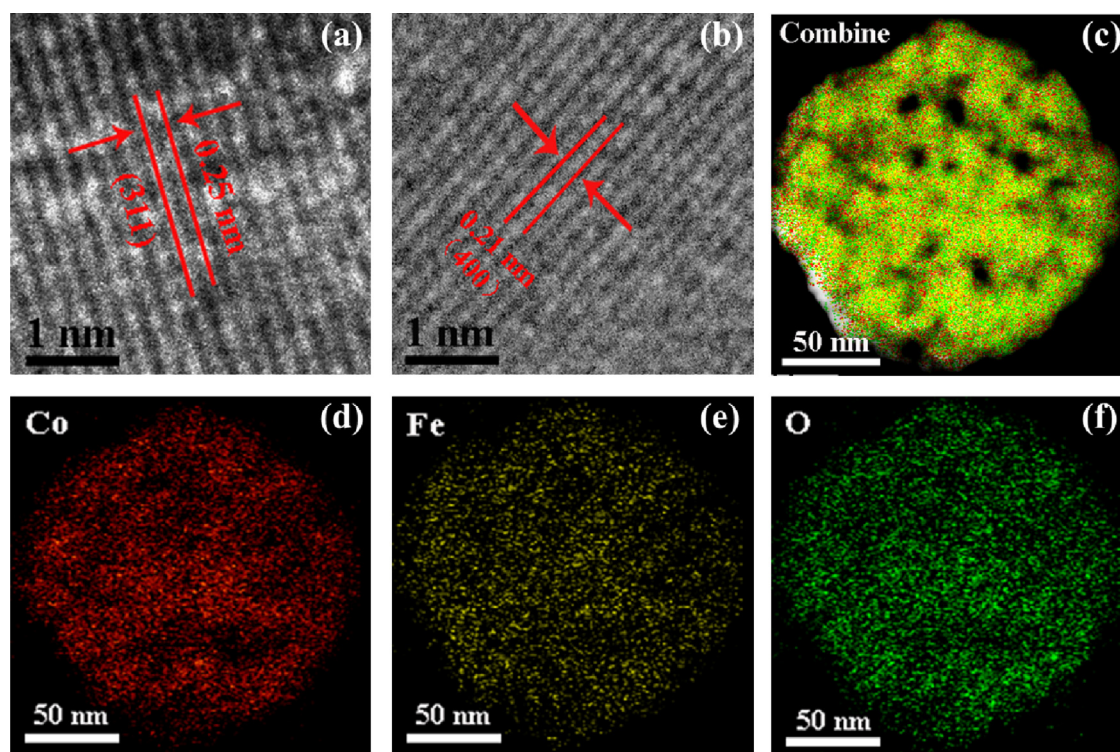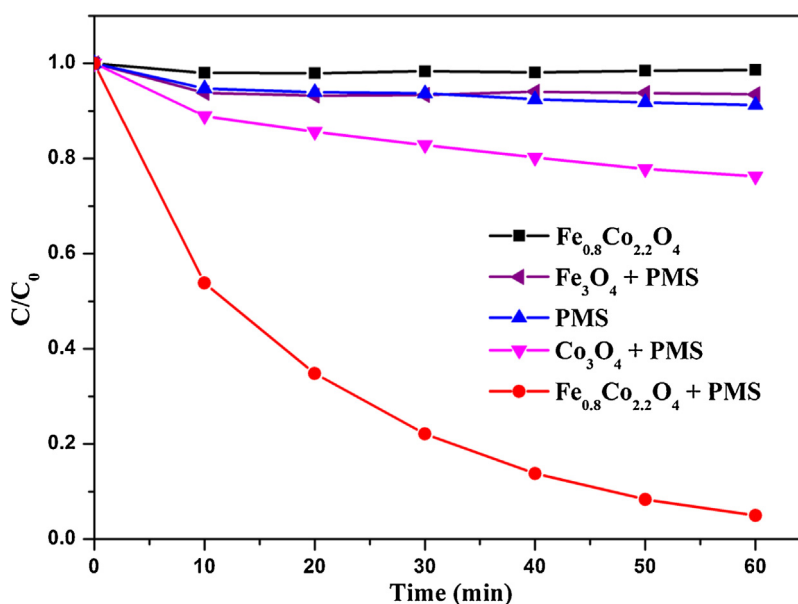**Fig. 5.** HR-TEM images (a, b) and EDX mappings of porous $Fe_{0.8}Co_{2.2}O_4$ nanocages (c–f).

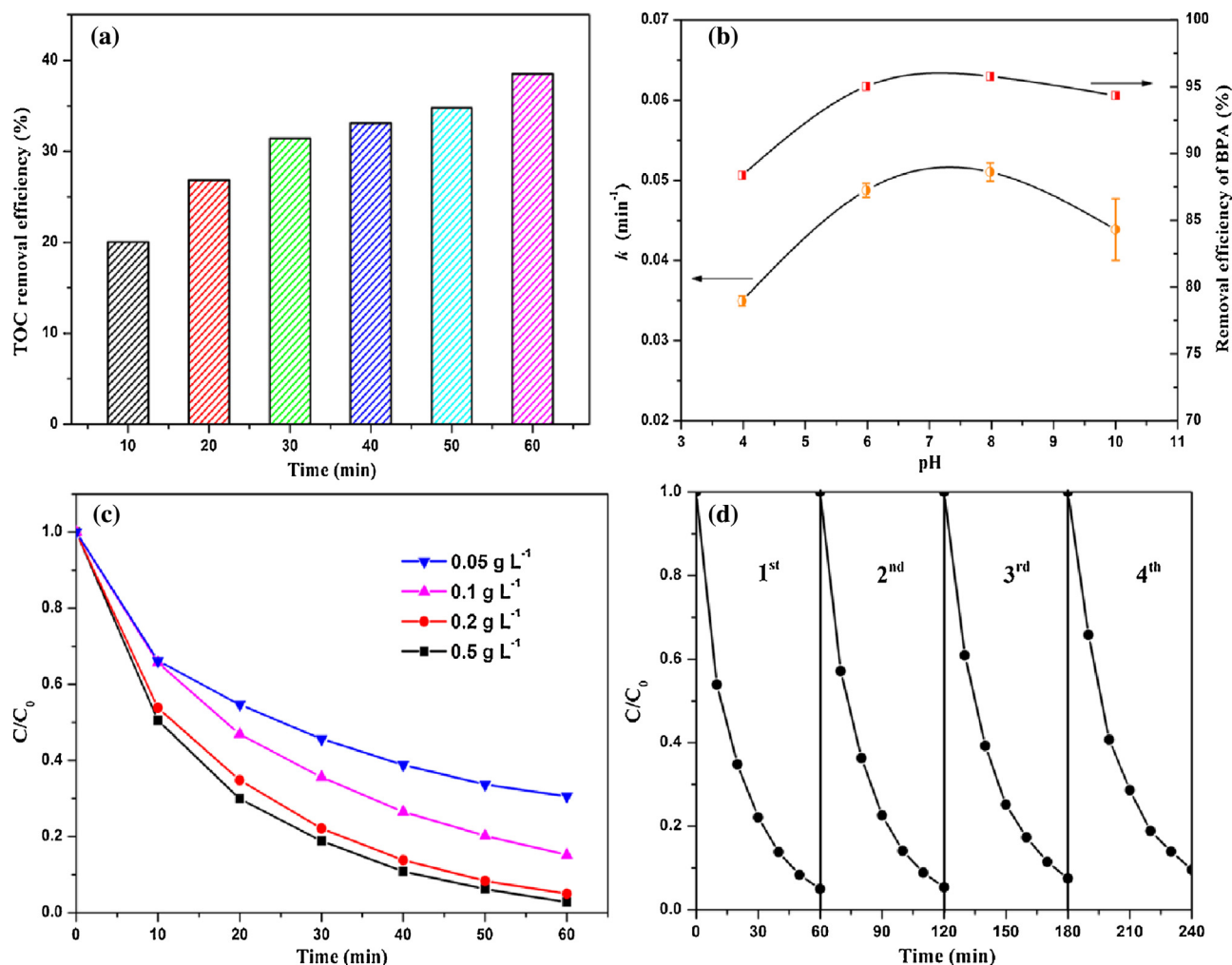**Fig. 6.** Removal efficiency of BPA in different reaction systems within 60 min. Reaction conditions: [BPA] = 20 mg L^{-1}, [PMS] = 0.2 g L^{-1} (if needed), catalyst = 0.1 g L^{-1}, T = 298 K, initial solution pH 6.0.

of the pH to 10.0 reduced this value to 0.044 min^{-1}. The oxidation ability of PMS for the degradation of BPA at different initial pH without catalyst was also examined (Fig. S7). Negligible changes of the removal efficiency could be observed under different pH condition (less than 10%), suggesting that the pH dependence phenomenon was mainly caused by the catalytic reaction over $Fe_{0.8}Co_{2.2}O_4$ surface. This phenomenon could be explained as follows: when initial pH < 8.0, the protonated surface of $Fe_xCo_{3-x}O_4$ was positively charged (pH$_{zpc}$ of $Fe_xCo_{3-x}O_4$ is about 5.0–7.0 [45]). Therefore, more HSO$_5^-$ could be absorbed onto the catalyst surface, promoting

the formation of radical intermediates (SO$_4^{\bullet-}$, HO$^{\bullet}$). Moreover, the increasing OH$^-$ concentration could also accelerate the decomposition of PMS to form radical intermediates. However, the surface of the catalyst became deprotonated when initial pH > 8.0, which was unfavorable for the absorption of HSO$_5^-$ onto $Fe_xCo_{3-x}O_4$ surface and thus reduced the reaction rate [19]. The results demonstrated the advantage of $Fe_xCo_{3-x}O_4$ nanocages to degrade organic compounds at neutral pH condition.

The effect of PMS concentration on the degradation of BPA was examined and the results are presented in Fig. 7c. As can be seen, the BPA removal efficiency increased with the increase of the PMS

Fig. 7. (a) TOC removal efficiency of BPA in the different reaction time; Effect of (b) initial pH and (c) PMS concentration on BPA removal efficiency; (d) Consecutive runs of the catalytic activities of $Fe_{0.8}Co_{2.2}O_4$. Reaction conditions: $[BPA] = 20\,mg\,L^{-1}$, $[PMS] = 0.2\,g\,L^{-1}$ (for a, b and d), catalyst = $0.1\,g\,L^{-1}$, $T = 298\,K$, initial solution pH 6.0 (for a, c and d).

concentration (0.05-$0.2\,g\,L^{-1}$). However, only slight increase could be observed with continued increasing the PMS concentration (0.2–$0.5\,g\,L^{-1}$). The optimum PMS concentration for the catalytic process could be explained by the competitive reactions which may adversely affect the generation of reactive species ($SO_4{}^{\bullet-} + SO_4{}^{\bullet-} \rightarrow SO_8{}^{2-}$, $HO^\bullet + SO_4{}^{\bullet-} \rightarrow HSO_5{}^-$) [46].

Finally, the operational stability of $Fe_{0.8}Co_{2.2}O_4$ nanocages was explored by testing the degradation of BPA in consecutive runs as shown in Fig. 7d. The result demonstrates that the regenerated catalyst exhibited good performance even after four-cycle runs. The slight loss of the catalytic activity was probably due to the adsorption of pollutants on the surface reactive sites of the $Fe_{0.8}Co_{2.2}O_4$ nanocages [47]. In addition, the leached Co and Fe were $0.36\,mg\,L^{-1}$ and $0.11\,mg\,L^{-1}$, respectively. These results demonstrate the high recyclability of $Fe_{0.8}Co_{2.2}O_4$ nanocages for pollutants degradation by activation of PMS.

3.3. Possible degradation pathway of BPA

To ascertain the BPA removal efficiency by activation of PMS on $Fe_{0.8}Co_{2.2}O_4$ nanocages, the BPA degradation intermediates were analyzed by GC–MS and LC–MS (Figs. S8–11). Twelve compounds, such as *p*-isopropenyl phenol, p-(alpha-Hydroxyethyl) phenol, 1-(2,4-dihydroxyphenyl) ethanone, etc. were identified in this work and listed in Table S2. The tentatively identified

intermediates such as phenol, 3,5-bis(1,1-dimethyl(ethyl)) and 4-isopropylenecatechol suggest that the phenoxyl (PhO) and iso-propenylphenol (IPP) radicals were probably involved in BPA degradation. Based on the present experimental results and the previous literatures [48–52], the proposed pathway of the degradation of BPA induced by activation of PMS over $Fe_xCo_{3-x}O_4$ nanocages is presented in Fig. 8. Firstly, the radicals attacked the aromatic ring and thus produced highly oxidizing phenoxyl BPA (PhxBPA), which could further form PhO and IPP radicals through the b-scission (C—C) (Route I). Meanwhile, an electrophilic $HO^\bullet$ group could be added onto the aromatic ring of the BPA, resulting in the formation of hydroxylated products such as BPA-O-catechol (Route II). Secondly, numbers of aromatic intermediates were formed through the hydroxylation, dehydration, oxidative skeletal rearrangement, etc. Finally, ring opening products, including oxalic, formic, acetic, alkane and propanoic acid ester were formed, which could be further mineralized into CO_2 and H_2O.

3.4. Reactive intermediates during PMS activation over $Fe_{0.8}Co_{2.2}O_4$ nanocages

The involved radical intermediates were probed by radical scavenger experiments. It is well accepted that PMS can generate $SO_4{}^{\bullet-}$ and/or $HO^\bullet$ during the activations [13,53]. When TBA, an effective radical scavenger for $HO^\bullet$ [54], was added to the reaction solution,
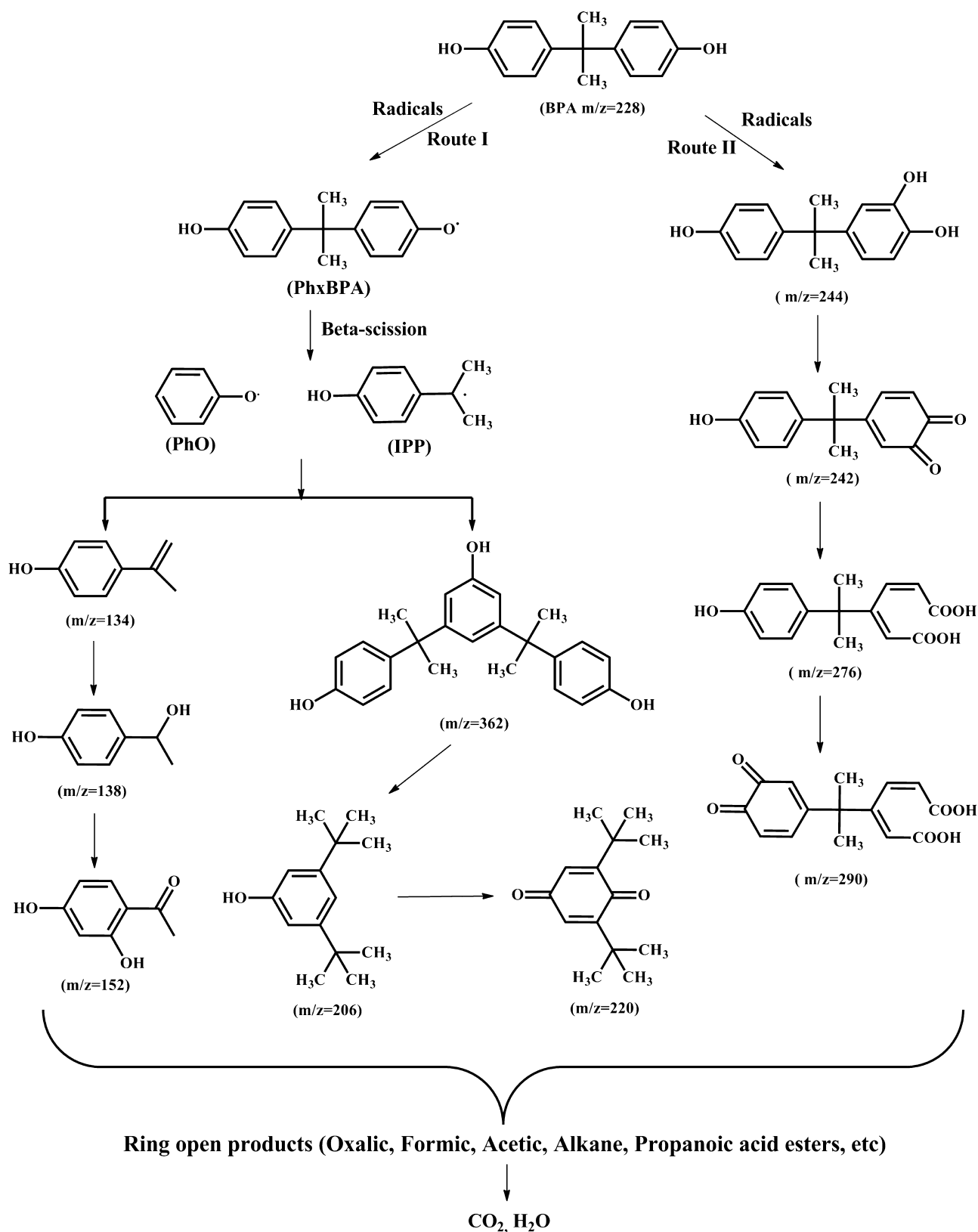
Fig. 8. Possible BPA degradation pathways by activation of PMS on $Fe_{0.8}Co_{2.2}O_4$ nanocages.

about 20% decrease of the reaction rate was observed (Fig. 9), indicating that the HO• might be one of the involved radical. However, when methanol, a widely used radical scavenger for both $SO_4^{•-}$ and HO• [55], was added to the reaction solution, more than 60%

decrease of the reaction rate was observed. Therefore, results suggest that the main radical intermediates involved in the activation of PMS by $Fe_{0.8}Co_{2.2}O_4$ nanocages were $SO_4^{•-}$ and HO•. In addition,
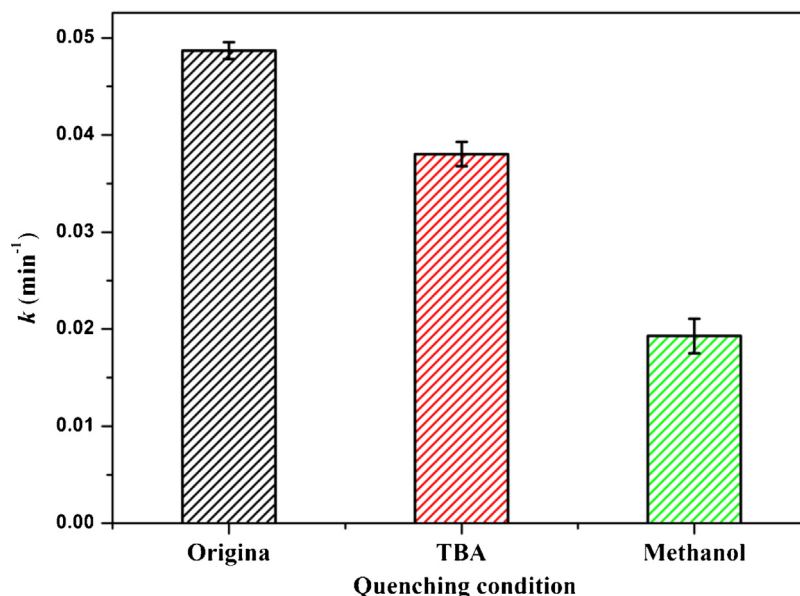
Fig. 9. Changes of reaction rate with and without radical scavengers of TBA and methanol. Reaction conditions: [BPA] = 20 mg L^{-1}, [PMS] = 0.2 g L^{-1}, catalyst = 0.1 g L^{-1}, [scavenger] = 0.2 M, T = 298 K, initial solution pH 6.0.

more remarkable reaction rate decrease was caused by methanol, indicating that SO$_4$•$^-$ may be a dominant reactive intermediate.

To further confirm the identity of the involved reactive intermediates, the EPR/DMPO experiments were carried out. As shown in Fig. 10a, no peaks were identified when BPA + DMPO system was tested, indicating that no radicals could be produced without PMS. However, when PMS + DMPO system was tested, characteristic signals for DMPO$^-$•OH adducts (with $a_N = a_H = 14.9$ G) were observed [56], suggesting the production of hydroxyl radicals by strong hydrolysis process of HSO$_5^-$ as shown in Eqs. 1–2 [43]. When BPA was added into the PMS + DMPO solution, the decrease relative intensity of DMPO-•OH signals suggests that the HO• radicals prefer to react with BPA rather than DMPO. However, the addition of Fe$_{0.8}$Co$_{2.2}$O$_4$ nanocages largely increased the relative intensity of the EPR signals, suggesting its excellent catalytic performance to activate PMS. The observed characteristic signals of DMPO-•OH adducts and DMPO- SO$_4$•$^-$ adducts (with $a_N = 13.2$ G and $a_H = 9.6$ G) reveal that both SO$_4$•$^-$ and HO• were generated during the activation of PMS by Fe$_{0.8}$Co$_{2.2}$O$_4$ nanocages [57].

$$HSO_{5-} + H_2O \leftrightarrow H_2O_2 + HSO_{4-} \quad (1)$$

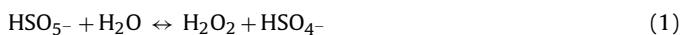$$H_2O_2 \rightarrow HO^\bullet + HO^\bullet \quad (2)$$

Fig. 10b shows the time-dependent relationship between BPA removal and the relative peak intensities of the DMPO-•OH /DMPO-SO$_4$•$^-$. The corresponding EPR spectra were shown in Fig. S12. As shown clearly, the DMPO-SO$_4$•$^-$ reached the highest peak intensity at about 5 min, when saturated HSO$_5^-$ was adsorbed on the catalyst surface. Then the gradually decreased DMPO-SO$_4$•$^-$ intensity indicates the continuous consumption of the SO$_4$•$^-$ radicals for BPA removal. However, the evolution of the DMPO-•OH intensity remained at a relative higher value and almost no change. These results further confirm that SO$_4$•$^-$ was the dominant radical involved in activation of PMS by Fe$_{0.8}$Co$_{2.2}$O$_4$ nanocages.

3.5. Activation mechanism of PMS over Fe$_{0.8}$Co$_{2.2}$O$_4$ nanocages

The ^{57}Fe Mössbauer spectroscopy is an ideal technique for determining the coordination environment and oxidation state of iron ions in a solid [34,58]. The Mössbauer spectra of Fe$_{0.8}$Co$_{2.2}$O$_4$ nanocages before and after reaction were measured to clarify the

Table 2
Room temperature ^{57}Fe Mössbauer parameters of Fe$_{0.8}$Co$_{2.2}$O$_4$ nanocages obtained before and after the reaction.

Fe$_{0.8}$Co$_{2.2}$O$_4$	Assignment	IS(mm s^{-1})	QS(mm s^{-1})	Width(mm s^{-1})	Area(%)
Before reaction	Tetrahedral (green)	0.30	0.56	0.33	61
	Octahedral (blue)	0.29	1.06	0.54	39
After reaction	Tetrahedral (green)	0.31	0.52	0.39	62
	Octahedral (blue)	0.33	0.93	0.56	38

Experimental errors are ±0.02 mm s^{-1} for isomer shift (IS), ±0.03 mm s^{-1} for quadrupole splitting (QS) and 1% for relative area. IS is relative to α-iron foil.

role of iron ion in activation of PMS (Fig. 11). Due to the superparamagnetic effect of Fe$_{0.8}$Co$_{2.2}$O$_4$ nanocages [59], the spectra were fitted with two quadrupole doublets. According to the isomer shift (IS) and quadruple splitting (QS) as listed in Table 2, the blue and green doublets were assigned to the octahedral (B-site) and tetrahedral (A-site) Fe^{III} in Fe$_{0.8}$Co$_{2.2}$O$_4$ nanocages, respectively [60,61]. Negligible changes could be observed after the reaction. Considering that negligible changes could be observed for the BPA removal efficiency with the Fe content in Fe$_x$Co$_{3-x}$O$_4$ increasing (Fig. S13), the activity probably did not originate from the iron ions in Fe$_{0.8}$Co$_{2.2}$O$_4$ nanocages.

The XPS spectra of Fe$_{0.8}$Co$_{2.2}$O$_4$ nanocages before and after reaction were introduced to further explore the activation mechanism of PMS. Fig. 12a shows the high resolution XPS spectra of the Co 2p$_{3/2}$ on Fe$_{0.8}$Co$_{2.2}$O$_4$ surface before and after the catalytic oxidation process. Three peaks with binding energy positioned at 778.8, 779.6 and 781.2 eV, with relative contributions to the overall Co intensity of 35%, 45% and 20%, could be assigned to Co^{II} in B-site, A-site and Co^{III} in B-site, respectively [62]. However, the relative contributions of these three peaks after the oxidation reaction are 30%, 45%, and 25%. This result suggests that the oxidizing reaction occurs on the catalyst surface and B-site Co^{II} would provide the electrons, leading to the increase of Co^{III} in B-site. In order to keep the charge balance on the catalyst surface, the B-site Co^{III} would accept the electrons from the system, which indicates the involvement of Co^{II}–Co^{III}–Co^{II} redox cycles during the catalytic oxidation reaction [19].

Fig. 12b shows the high resolution XPS spectra of O 1s on Fe$_{0.8}$Co$_{2.2}$O$_4$ surface before and after the catalytic oxidation pro-

(a)

(b)
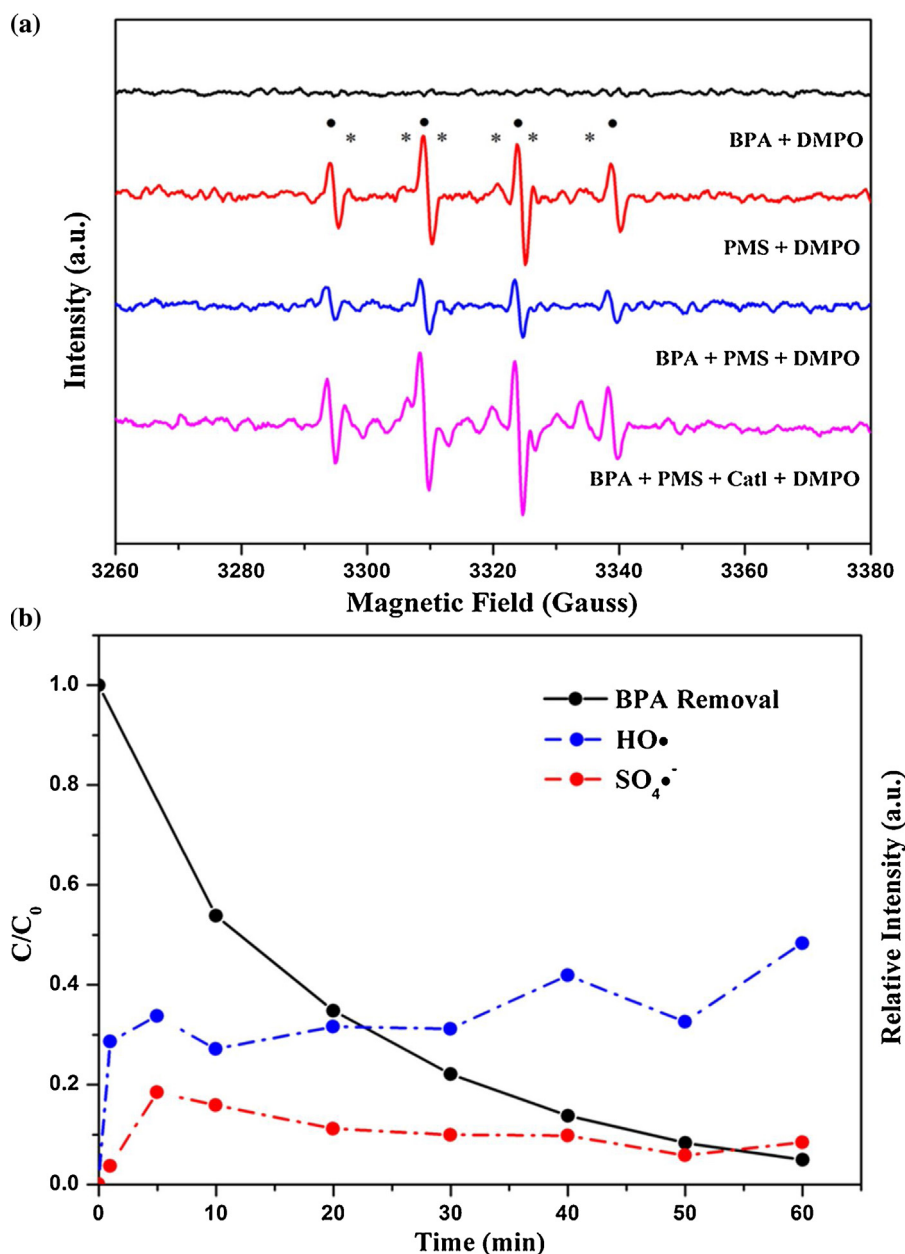
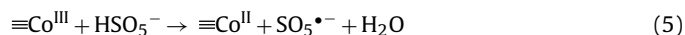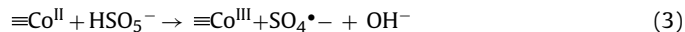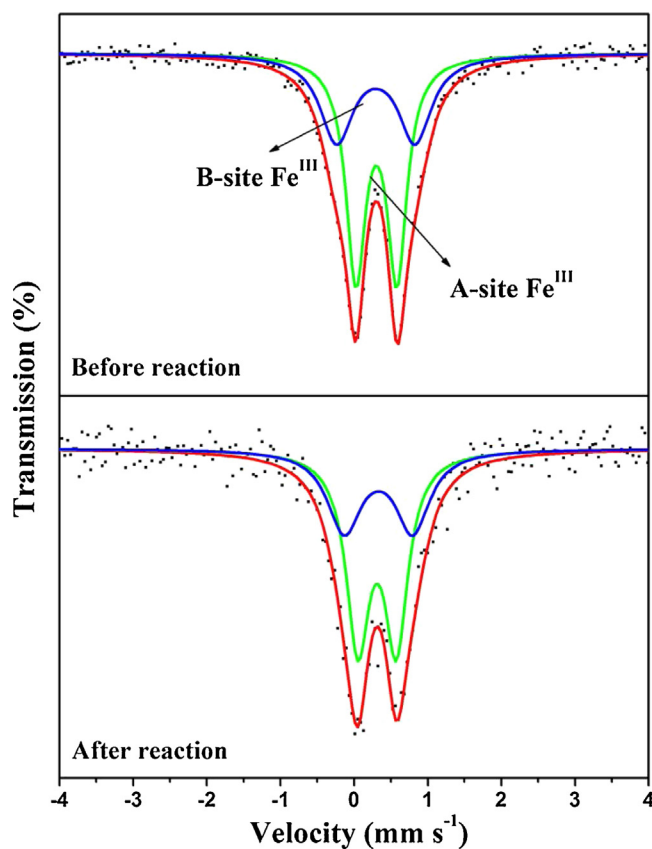
Fig. 10. (a) EPR spectra of various simulated systems; (b) BPA removal profile and relative intensity variations of DMPO-•OH and DMPO-SO$_4$•$^-$ during reaction. Reaction conditions: [BPA] = 20 mg L^{-1}, [PMS] = 0.2 g L^{-1}, catalyst = 0.1 g L^{-1}, T = 298 K, initial solution pH 6.0.

cess. Two peaks with binding energy located at 528.6 and 530.1 eV, with relative contents of 67% and 33%, could be assigned to the lattice oxygen (O$_\beta$) and surface hydroxyl species or adsorbed oxygen (O$_\alpha$), respectively [62]. After the catalytic oxidation reaction, the relative contents of O$_\beta$ and O$_\alpha$ change to 59% and 41%, respectively, The decrease of Oβ might be due to its oxidization to O$_2$ caused by the reduction of Co^{III} to Co^{II} [63], which suggests the involvement of O$_\beta$ in the catalytic cycling. The slight changes observed from the high resolution XPS spectra of Fe^{III} could be also ascribed to this release of O$_2$ (Fig. S14). All these results demonstrate that B-site Co^{II} on the catalyst surface was the main factor for the excellent activity and the O$_\beta$ was involved.

Therefore, the overall activation mechanism of PMS over Fe$_{0.8}$Co$_{2.2}$O$_4$ nanocages could be proposed as follows (Eqs. (3)–(6)). Firstly, the HSO$_5$$^-$ species were adsorbed onto the surface of the catalyst and activated by B-site Co^{II} to produce SO$_4$•$^-$ radicals (Eq. (3)). At the same time, HO• radicals could be also produced through Eq.

4. These involved radicals could degrade the BPA to small organic intermediates or even CO$_2$ (Eq. (7)). Secondly, in order to keep the charge balance on the catalyst surface, B-site Co^{II} would accept the electrons from the O$_\beta$ in the system (Eqs. (5), (6)) and reduced to Co^{II}. Furthermore, the comparison of the redox potential could further support the proposed mechanism. The potential value of Co^{II}/Co^{III} redox pair (1.8 V), which is between that of HSO$_5$$^-$/SO$_4$•$^-$ (2.5–3.1 V) and HSO$_5$$^-$/SO$_5$•$^-$ (1.1 V), makes its redox cycling thermodynamically feasible in the activation of PMS (Eqs. (3), (5)) [12]. However, for redox pair Fe^{II}/Fe^{III} (0.8 V), which demonstrates a negative redox potential of −0.3 V compared to HSO$_5$$^-$/SO$_5$•$^-$, results in its redox cycling thermodynamically unfavorable [64].

$$\equiv Co^{II} + HSO_5^- \rightarrow \equiv Co^{III} + SO_4^{\bullet-} + OH^- \tag{3}$$

$$SO_4^{\bullet-} + OH^- \rightarrow SO_4^{2-} + HO^{\bullet} \tag{4}$$

$$\equiv Co^{III} + HSO_5^- \rightarrow \equiv Co^{II} + SO_5^{\bullet-} + H_2O \tag{5}$$

Fig. 11. Room temperature ^{57}Fe Mössbauer spectra of $Fe_{0.8}Co_{2.2}O_4$ nanocages before and after reaction. The spectra were fitted with two quadrupole doublets. The blue and green doublets were assigned to the octahedral-site (B-site) and tetrahedral-site (A-site) Fe^{III} in $Fe_{0.8}Co_{2.2}O_4$ nanocages, respectively.
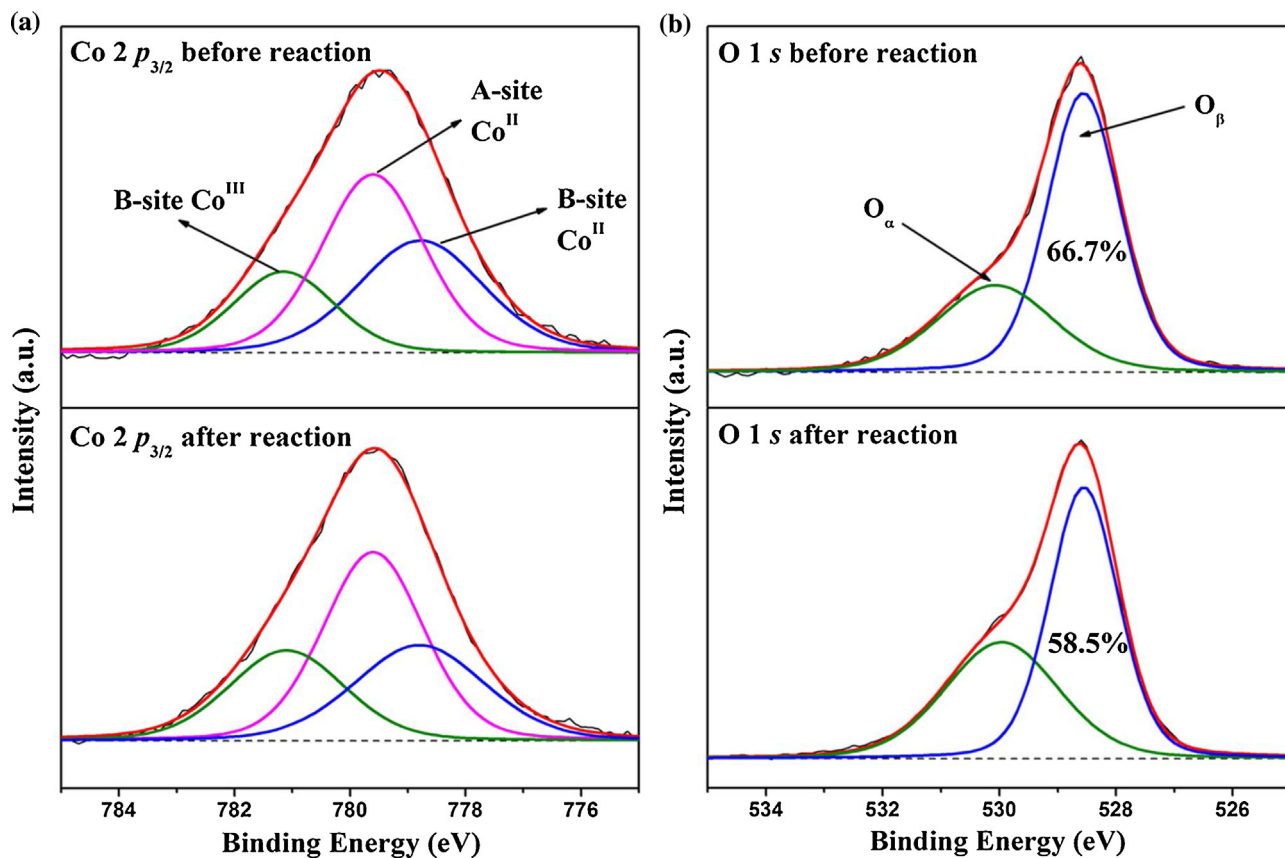
Fig. 12. High resolution XPS spectra of (a) Co $2p_{3/2}$ and (b) O 1s in $Fe_{0.8}Co_{2.2}O_4$ nanocages before and after reaction.

$$SO_5^{\bullet-} + O_\beta \rightarrow SO_4^{\bullet-} + O_2 \tag{6}$$

$$SO_4^{\bullet-}/HO^\bullet + BPA \rightarrow CO_2 + intermediates \tag{7}$$

4. Conclusions

Porous $Fe_xCo_{3-x}O_4$ nanocages were synthesized via a facile strategy by heating Fe_yCo_{1-y}–Co PBAs nanospheres with tunable size and morphology. The iron doping amount was found to have a significant influence on the final morphology and $Fe_{0.8}Co_{2.2}O_4$ appeared to be most uniform. The prepared $Fe_xCo_{3-x}O_4$ nanocages were found to be efficient to activate PMS into radicals, which could further degraded BPA to small organic compounds or even inorganic carbon forms. Through radical scavenger and EPR/DMPO experiments, both $SO_4^{\bullet-}$ and $HO^\bullet$ radicals were proved to be involved and the former plays a more critical role during the activation of PMS. Based on the GC–MS and LC-MS results, the BPA degradation pathway which involved PhO and IPP radicals as the intermediates was proposed. The catalyst was shown to be stable and reusable even after a four-cycle test. The higher reaction temperature and PMS concentration could accelerate the reaction rate and the neutral pH (6–8) was found to be most suitable for PMS activation. The activation mechanism of PMS over $Fe_{0.8}Co_{2.2}O_4$ nanocages was explored and B-site Co^{II} on the catalyst surface was determined as the main factor for the excellent activity. This study may expand the further development of the porous MTMOs-type heterogeneous catalysts for the degradation of organic pollutants by activation of PMS.

Acknowledgements

Appendix A. Supplementary data

Supplementary data associated with this article can be found, in the online version, at http://dx.doi.org/10.1016/j.apcatb.2015.08.050.

References

[1] C.A. Staples, P.B. Dorn, G.M. Klecka, S.T. O'Block, L.R. Harris, Chemosphere 36 (1998) 2149.
[2] J.-H. Kang, F. Kondo, Y. Katayama, Toxicology 226 (2006) 79.
[3] L.N. Nguyen, F.I. Hai, S. Yang, J. Kang, F.D.L. Leusch, F. Roddick, W.E. Price, L.D. Nghiem, Bioresour. Technol. 148 (2013) 234.
[4] W.T. Tsai, C.W. Lai, T.Y. Su, J. Hazard. Mater. 134 (2006) 169.
[5] B. Gao, T.M. Lim, D.P. Subagio, T.-T. Lim, Appl. Catal. A- Gen. 375 (2010) 107.
[6] S. Enami, Y. Sakamoto, A.J. Colussi, Proc. Natl. Acad. Sci. U. S. A. 111 (2014) 623.
[7] X.J. Yang, X.M. Xu, J. Xu, Y.F. Han, J. Am. Chem. Soc. 135 (2013) 16058.
[8] P.V. Nidheesh, R. Gandhimathi, S.T. Ramesh, Environ. Sci. Pollut. Res. Int. 20 (2013) 2099.
[9] C. Wang, H. Liu, Z. Sun, Int. J. Photoenergy (2012) 801694.
[10] X. Zhang, Y. Ding, H. Tang, X. Han, L. Zhu, N. Wang, Chem. Eng. J. 236 (2014) 251.
[11] P. Neta, R.E. Huie, A.B. Ross, J. Phys. Chem. Ref. Data 17 (1988) 1027.
[12] G.P. Anipsitakis, D.D. Dionysiou, Environ. Sci. Technol. 37 (2003) 4790.
[13] Q. Yang, H. Choi, S.R. Al- Abed, D.D. Dionysiou, Appl. Catal. B 88 (2009) 462.
[14] Y. Ding, L. Zhu, A. Huang, X. Zhao, X. Zhang, H. Tang, Catal. Sci. Technol. 2 (2012) 1977.
[15] J. Deng, Y. Shao, N. Gao, C. Tan, S. Zhou, X. Hu, J. Hazard. Mater. 262 (2013) 836.
[16] W. Li, P. Wu, S. Yang, Y. Zhu, C. Kang, L.T. Tran, B. Zeng, RSC Adv. 5 (2015) 8859.
[17] Y. Yao, Y. Cai, G. Wu, F. Wei, X. Li, H. Chen, S. Wang, J. Hazard. Mater. 296 (2015) 128.
[18] S. Su, W. Guo, Y. Leng, C. Yi, Z. Ma, J. Hazard. Mater. 244 (2013) 736.
[19] Y. Ren, L. Lin, J. Ma, J. Yang, J. Feng, Z. Fan, Appl. Catal. B 165 (2015) 572.
[20] M. Stoyanova, I. Slavova, S. Christoskova, V. Ivanova, Appl. Catal. A- Gen. 476 (2014) 121.
[21] T. Zeng, X. Zhang, S. Wang, H. Niu, Y. Cai, Environ. Sci. Technol. 49 (2015) 2350.
[22] Y.-P. Zhu, T.-Z. Ren, Z.-Y. Yuan, RSC Adv. 5 (2015) 7628.
[23] Y.-P. Zhu, T.-Z. Ren, Z.-Y. Yuan, Nanoscale 6 (2014) 11395.
[24] Y.-P. Zhu, T.-Z. Ren, Z.-Y. Yuan, Catal. Sci. Technol. (2015), http://dx.doi.org/10.1039/C5CY00107B.
[25] Z.P. Niu, Y. Wang, F.S. Li, J. Mater. Sci 41 (2006) 5726.
[26] R.T. Olsson, G. Salazar-Alvarez, M.S. Hedenqvist, U.W. Gedde, F. Lindberg, S.J. Savage, Chem. Mater. 17 (2005) 5109.
[27] X. Wang, J. Zhuang, Q. Peng, Y.D. Li, Nature 437 (2005) 121.
[28] X. Li, J. Liu, A.I. Rykov, H. Han, C. Jin, X. Liu, J. Wang, Appl. Catal. B 179 (2015) 196.
[29] L. Hu, Q. Chen, Nanoscale 6 (2014) 1236.
[30] L. Zhang, H.B. Wu, X.W. Lou, J. Am. Chem. Soc. 135 (2013) 10664.
[31] S.J. Yang, S. Nam, T. Kim, J.H. Im, H. Jung, J.H. Kang, S. Wi, B. Park, C.R. Park, J. Am. Chem. Soc. 135 (2013) 7394.
[32] M.B. Zakaria, M. Hu, M. Imura, R.R. Salunkhe, N. Umezawa, H. Hamoudi, A.A. Belik, Y. Yamauchi, Chem. -Eur. J. 20 (2014) 17375.
[33] C. Yuan, H.B. Wu, Y. Xie, X.W. Lou, Angew. Chem. Int. Ed. 53 (2014) 1488.
[34] X. Li, J. Wang, A.I. Rykov, V.K. Sharma, H. Wei, C. Jin, X. Liu, M. Li, S. Yu, C. Sun, D.D. Dionysiou, Catal. Sci. Technol. 5 (2015) 504.
[35] Y.F. Gao, C.X. Cao, L. Dai, H.J. Luo, M. Kanehira, Y. Ding, Z.L. Wang, Energy Environ. Sci. 5 (2012) 8708.
[36] H. Guo, T. Li, W. Chen, L. Liu, X. Yang, Y. Wang, Y. Guo, Nanoscale 6 (2014) 15168.
[37] L. Hu, Y. Huang, Q. Chen, J. Alloys Compd. 559 (2013) 57.
[38] J. Zhang, L. Wang, L. Xu, X. Ge, X. Zhao, M. Lai, Z. Liu, W. Chen, Nanoscale 7 (2015) 720.
[39] L. Zhang, L. Shi, L. Huang, J. Zhang, R. Gao, D. Zhang, ACS Catal. 4 (2014) 1753.
[40] L. Zhou, D. Zhao, X.W. Lou, Adv. Mater. 24 (2012) 745.
[41] H.B. Wu, H. Pang, X.W. Lou, Energy Environ. Sci. 6 (2013) 3619.
[42] W.-D. Oh, S.-K. Lua, Z. Dong, T.-T. Lim, J. Mater. Chem. A 2 (2014) 15836.
[43] Y. Wang, H. Sun, H.M. Ang, M.O. Tade, S. Wang, ACS Appl. Mater. Interfaces 6 (2014) 19914.
[44] P.R. Shukla, S. Wang, H. Sun, H.M. Ang, M. Tadé, Appl. Catal. B 100 (2010) 529.
[45] M. Barale, C. Mansour, F. Carrette, E.M. Pavageau, H. Catalette, G. Lefèvre, M. Fedoroff, G. Cote, J. Nucl. Mater. 381 (2008) 302.
[46] Y. Wang, S. Indrawirawan, X. Duan, H. Sun, H.M. Ang, M.O. Tadé, S. Wang, Chem. Eng. J. 266 (2015) 12.
[47] Y. Wang, H. Sun, H.M. Ang, M.O. Tadé, S. Wang, Appl. Catal. B 164 (2015) 159.
[48] J. Sharma, I.M. Mishra, D.D. Dionysiou, V. Kumar, Chem. Eng. J. 276 (2015) 193.
[49] X. Wang, Y. Qin, L. Zhu, H. Tang, Environ. Sci. Technol. 49 (2015) 6855.
[50] J. Poerschmann, U. Trommler, T. Górecki, Chemosphere 79 (2010) 975.
[51] W. Li, Y. Wu, Z.-j. Huang, Y.-h. Lu, Y.-w. Li, Z. Dang, N.-w. Zhu, Chem. Eng J. 279 (2015) 93.
[52] Y. Ding, L. Zhu, N. Wang, H. Tang, Appl. Catal. B 129 (2013) 153.
[53] G.P. Anipsitakis, D.D. Dionysiou, M.A. Gonzalez, Environ. Sci. Technol. 40 (2006) 1000.
[54] J. Benner, T.A. Ternes, Environ. Sci. Technol. 43 (2009) 5472.
[55] Y.-H. Guan, J. Ma, X.-C. Li, J.-Y. Fang, L.-W. Chen, Environ. Sci. Technol. 45 (2011) 9308.
[56] W.H. Ma, J. Li, X. Tao, J. He, Y.M. Xu, J.C. Yu, J.C. Zhao, Angew. Chem. Int. Ed. 42 (2003) 1029.
[57] G.-D. Fang, D.D. Dionysiou, S.R. Al- Abed, D.-M. Zhou, Appl. Catal. B 129 (2013) 325.
[58] A.I. Rykov, X. Li, J. Wang, J. Solid State Chem. 227 (2015) 35.
[59] B. Pandey, F.J. Litterst, E.M. Baggio-Saitovitch, J. Magn. Magn. Mater. 385 (2015) 412.
[60] D. Vanidha, A. Arunkumar, S.N. Achary, S. Rajagopan, R. Kannan, J. Mol. Struct. 1076 (2014) 105.
[61] K. Krieble, T. Schaeffer, J.A. Paulsen, A.P. Ring, C.C.H. Lo, J.E. Snyder, J. Appl. Phys. 97 (2005) 107101.
[62] Z. Zhou, Y. Zhang, Z. Wang, W. Wei, W. Tang, J. Shi, R. Xiong, Appl. Surf. Sci. 254 (2008) 6972.
[63] R. Polniser, M. Stolcova, M. Hronec, M. Mikula, Appl. Catal. A- Gen. 400 (2011) 122.
[64] Y. Zhong, X. Liang, W. Tan, Y. Zhong, H. He, J. Zhu, P. Yuan, Z. Jiang, J. Mol. Catal. A: Chem. 372 (2013) 29.